Topological phase transitions by time-dependent electromagnetic fields in frustrated magnets: Role of dynamical and static magnetic fields

Tatsuya Shirato,[1,*] Ryota Yambe,[2] and Satoru Hayami[1,†]

[1] *Graduate School of Science, Hokkaido University, Sapporo 060-0810, Japan*
[2] *Department of Applied Physics, The University of Tokyo, Tokyo 113-8656, Japan*

(Dated: May 22, 2026)

We theoretically investigate the effects of time-dependent electromagnetic fields on frustrated magnets with the spatial inversion symmetry. Two types of external-field setups are considered: One is a circularly polarized electromagnetic field and the other is a combination of a circularly polarized electric field and a static magnetic field. The system is modeled by a classical frustrated Heisenberg model on a triangular lattice, whose ground state is a single-Q spiral spin configuration. The effects of irradiated electric and magnetic fields are taken into account by the inverse Dzyaloshinskii–Moriya (DM) interaction and the Zeeman coupling, respectively, without heating effects. By numerically solving the Landau–Lifshitz–Gilbert equation, we find that the two field configurations lead to distinct skyrmion crystal (SkX) phases and their associated topological phase transitions: in the former setup, SkXs composed of skyrmions with skyrmion numbers of one and two with opposite signs emerge, whereas in the latter setup, SkXs with the same sign appear. The stabilization mechanisms of these SkXs are accounted for by the competition among electromagnetic-field-induced chiral DM interactions, electric-field-induced three-spin interactions, and the Zeeman coupling based on the high-frequency expansion within the Floquet formalism. Furthermore, for the latter setup, we find that the stability region of the SkX phase varies significantly depending on the timing of the application of the circularly polarized electric field and the static magnetic field. Our findings would broaden the possible routes to generate and control SkXs by time-dependent electromagnetic fields, advancing both the theoretical comprehension and experimental control of topological spin crystals.

I. INTRODUCTION

The concept of topology has attracted tremendous interest due to its fundamental significance in physics. The study of topology in condensed matter systems may be broadly classified into two categories: topology in real space and that in reciprocal space. The pioneering studies of the former can be traced back to the discovery of the Kosterlitz-Thouless transition [1, 2], whereas those of the latter originate from the foundation of Thouless-Kohmoto-Nightingale-den Nijs formula [3, 4]. In the context of the real-space topology, skyrmions, characterized by an integer topological number called a skyrmion number, have been studied both theoretically and experimentally [5–13]. The skyrmion number corresponds to how many times the classical spins consisting of the skyrmion spin texture wrap a three-dimensional unit sphere. In magnetic materials, skyrmions often emerge as periodic alignments, the so-called skyrmion crystals (SkXs), composed of superpositions of multiple spiral spin density waves with symmetry-related ordering wave vectors, i.e., the multiple-Q state. Their topological nature gives rise to a fictitious electromagnetic field via the Berry phase mechanism [14], which generates exotic quantum transport phenomena [15–20]. Magnetic skyrmions are promising candidates for building highly integrated and low-power neuromorphic devices that specialize in running artificial neural network models [21, 22]. Because of their nanoscale size and low-power operation compared to conventional spin textures, they are expected to serve effectively as physical reservoirs in reservoir computing systems [23].

SkXs have been discovered in various magnets without spatial inversion symmetry since the first experimental report in chiral magnets MnSi [19, 24, 25] and $Fe_{1-x}Co_xSi$ [26, 27]. They are stabilized by the competition between the ferromagnetic exchange interaction and the Dzyaloshinskii–Moriya (DM) interaction [8, 28], the latter of which arises from the relativistic spin–orbit coupling [29, 30]. Meanwhile, the formation of SkXs has also been demonstrated in centrosymmetric magnets, where the first experimental demonstration has been done in Gd_2PdSi_3 [31] and $Gd_3Ru_4Al_{12}$ [32, 33]. In such systems, the geometrically frustrated interaction or the Ruderman–Kittel–Kasuya–Yosida (RKKY) interaction [34–36] leads to competing exchange interactions among spins, which can be a source of multiple-Q states. Upon applying external stimuli such as magnetic fields or thermal fluctuations, these frustrated systems can undergo phase transitions into SkX states, where the external effects play a crucial role in their formation [37–42]. Most of the previous theoretical studies have focused on the role of the Zeeman coupling under static magnetic fields [7, 8, 43]. In recent years, increasing attention has been paid to the realization and control of SkXs through electric fields [44]. In particular, in certain multiferroic materials, electric fields couple directly to spins [45], giving rise to various phenomena such as the creation of

* tshirato@phys.sci.hokudai.ac.jp
† hayami@phys.sci.hokudai.ac.jp

skyrmions by electric-field pulses [46–48] and the stabilization of SkX phases under circularly or linearly polarized electric fields [49, 50].

In this paper, we investigate non-equilibrium steady states (NESSs) induced by time-dependent electromagnetic fields in frustrated magnets. Specifically, we consider two setups on external fields: (i) a circularly polarized electromagnetic field and (ii) a combination of a circularly polarized electric field and a static magnetic field. We irradiate these time-dependent electromagnetic fields with a classical frustrated Heisenberg model on a triangular lattice, whose ground state is a single-Q spiral state. The electric field is assumed to couple to the spin degree of freedom via the inverse DM mechanism [51, 52]. By solving the Landau–Lifshitz–Gilbert (LLG) equation under the applied electromagnetic fields without including heating effects, qualitatively different results are obtained for the two setups. Under circularly polarized electromagnetic irradiation, SkXs composed of skyrmions with the skyrmion numbers of one and two but with opposite signs are generated. In contrast, when both a circularly polarized electric field and a static magnetic field are simultaneously applied, SkXs with the same sign skyrmion number are formed. The stabilization mechanisms of the obtained SkXs in each case can be elucidated in terms of electromagnetic-field-induced chiral DM interactions, electric-field-induced three-spin interactions, and the Zeeman coupling to the magnetic fields within the high-frequency expansion in the Floquet formalism. Furthermore, for the second setup, our results reveal that the stability window of the SkX phase strongly depends on when the circularly polarized electric field and the static magnetic field are applied.

While previous studies based on the Floquet formalism have clarified the emergence of effective interactions under high-frequency electromagnetic fields [51], most of them have focused on equilibrium or effective static descriptions. In contrast, the present study addresses the NESSs of classical spin systems, where the real-time dynamics and dissipation play essential roles. In particular, we demonstrate that the interplay between time-dependent fields and dissipative dynamics leads to a systematic selection of topological spin textures with different skyrmion numbers, including higher-order SkXs with the skyrmion number of two, which cannot be trivially inferred from equilibrium effective Hamiltonians alone. Furthermore, we uncover that the timing and combination of external fields provides an additional control knob, giving rise to path-dependent stabilization of SkXs. This highlights a fundamentally dynamical mechanism beyond conventional Floquet engineering.

The rest of this paper is organized as follows. In Sec. II, we introduce the classical Heisenberg model with frustrated exchange interactions and extend it to include the effects of time-dependent electromagnetic fields. Then, we outline the method based on the LLG equation in Sec. III. In Sec. IV, we show the simulation results for the right circularly polarized (RCP) electric field. Finally, Sec. V is devoted to the summary. The frequency dependence of obtained results is summarized in Appendix A. The simulation results for the left circularly polarized (LCP) electric field are shown in Appendix B.

II. MODEL

We consider a classical Heisenberg model with frustrated exchange interactions on the two-dimensional triangular lattice, which is given by

$$\mathcal{H}_0 = -J_1 \sum_{\langle i,j\rangle} \boldsymbol{S}_i \cdot \boldsymbol{S}_j - J_3 \sum_{\langle\langle i,j\rangle\rangle} \boldsymbol{S}_i \cdot \boldsymbol{S}_j, \tag{1}$$

where $\boldsymbol{S}_i = (S_i^x, S_i^y, S_i^z)$ represents the localized spin at site i with $|\boldsymbol{S}_i| = 1$. The Hamiltonian consists of the ferromagnetic exchange interaction between the nearest-neighbor spins $\langle i,j\rangle$, $J_1 > 0$, and the antiferromagnetic exchange interaction between the third-neighbor spins $\langle\langle i,j\rangle\rangle$, $J_3 < 0$. We set the lattice constant to unity $a = 1$. For $J_1/|J_3| < 4$, the ground state is the single-Q spiral state with the ordering wave vector $|\boldsymbol{Q}^*| = Q^* = 2\cos^{-1}[(1+\sqrt{1-2J_1/J_3})/4]$. There are six equivalent ordering wave vectors; $\pm\boldsymbol{Q}_1^* = \pm Q^*(1,0)$, $\pm\boldsymbol{Q}_2^* = \pm Q^*(-1/2, \sqrt{3}/2)$, and $\pm\boldsymbol{Q}_3^* = \pm Q^*(-1/2, -\sqrt{3}/2)$.

We apply external electromagnetic fields on the model in Eq. (1). The model Hamiltonian is given by

$$\mathcal{H}(t) = \mathcal{H}_0 - \boldsymbol{E}(t) \cdot \sum_{\langle i,j\rangle} \boldsymbol{p}_{ij} - \boldsymbol{B}(t) \cdot \sum_i \boldsymbol{S}_i, \tag{2}$$

The second term in Eq. (2) represents the coupling of the electric field $\boldsymbol{E}(t)$ to the electric dipole $\boldsymbol{p}_{ij}$ between the nearest-neighbor bond; a circularly polarized electric field is given by $\boldsymbol{E}(t) = E_0(\delta\cos\omega t, -\sin\omega t, 0)$ with the strength E_0, the frequency ω, and the periodicity $T = 2\pi/\omega$. $\delta = +1$ (-1) stands for the right (left) circular polarization. The electric dipole is activated by the inverse DM mechanism in the form of $\boldsymbol{p}_{ij} = -\lambda \boldsymbol{e}_{ij} \times (\boldsymbol{S}_i \times \boldsymbol{S}_j)$ with the magnetoelectric coupling constant λ and the unit bond vector $\boldsymbol{e}_{ij}$ [45, 53–55]; we ignore other symmetry-allowed couplings between the electric field and electric dipoles [52]. The third term in Eq. (2) describes the Zeeman coupling to the magnetic field $\boldsymbol{B}(t)$. We consider two types of magnetic fields: One is the circularly polarized magnetic field $(-B_0\sin\omega t, -\delta B_0\cos\omega t, 0)$ with the strength B_0 and the other is the static magnetic field $(0, 0, B_{\rm s}^z)$ with the strength $B_{\rm s}^z$, namely, $\boldsymbol{B}(t) = (-B_0\sin\omega t, -\delta B_0\cos\omega t, B_{\rm s}^z)$.

III. METHOD

To obtain NESSs, which is defined as a state exhibiting temporal fluctuations around a steady time-averaged value, in Eq. (2), we solve the LLG equation by ignoring heating effects. The LLG equation is given by

$$\frac{d\boldsymbol{S}_i}{dt} = -\frac{\gamma}{1+\alpha_{\mathrm{G}}^2}\left\{\boldsymbol{S}_i \times \boldsymbol{B}_i^{\mathrm{eff}}(t) + \alpha_{\mathrm{G}}\,\boldsymbol{S}_i \times [\boldsymbol{S}_i \times \boldsymbol{B}_i^{\mathrm{eff}}(t)]\right\}, \tag{3}$$

with the gyromagnetic ratio γ, the Gilbert damping constant α_{G}, and the effective magnetic field $\boldsymbol{B}_i^{\mathrm{eff}}(t) = -\partial\,\mathcal{H}(t)/\partial \boldsymbol{S}_i$.

While solving the LLG equation, we calculate the local scalar spin chirality, which is given by $\chi_{\boldsymbol{r}}(t) = \boldsymbol{S}_i(t)\cdot[\boldsymbol{S}_j(t)\times\boldsymbol{S}_k(t)]$, where sites i, j, and k form the triangle at the position vector $\boldsymbol{r}$ in counterclockwise order. The skyrmion number for the whole system on a discrete lattice is given by

$$N_{\mathrm{sk}}(t) = \frac{1}{4\pi}\sum_{\boldsymbol{r}}\Theta_{\boldsymbol{r}}(t), \tag{4}$$

with a skyrmion density $\Theta_{\boldsymbol{r}}(t) \in [-2\pi, 2\pi)$ [56];

$$\tan\frac{\Theta_{\boldsymbol{r}}(t)}{2} = \frac{2\chi_{\boldsymbol{r}}(t)}{[\boldsymbol{S}_i(t)+\boldsymbol{S}_j(t)+\boldsymbol{S}_k(t)]^2-1}. \tag{5}$$

The skyrmion number in the magnetic unit cell (the number of magnetic unit cells: N_{unit}) is defined as $n_{\mathrm{sk}} = N_{\mathrm{sk}}/N_{\mathrm{unit}}$. In addition, we calculate the magnetization, which is given by

$$M^{\alpha}(t) = \frac{1}{N}\sum_i S_i^{\alpha}(t), \tag{6}$$

where N is the system size and $\alpha = x, y, z$. We also calculate the momentum decomposition of spins in reciprocal space, which is given by

$$S_{\boldsymbol{q}}(t) = \frac{1}{N}\sqrt{\sum_{\alpha,i,j} S_i^{\alpha}(t)S_j^{\alpha}(t)e^{i\boldsymbol{q}\cdot(\boldsymbol{R}_i-\boldsymbol{R}_j)}}, \tag{7}$$

where $\boldsymbol{q}$ is the wave vector and $\boldsymbol{R}_i$ is the position vector at the site i. The averages of these quantities are calculated once the system attains a NESS. By setting the time to reach the NESS as t_0, the averaged quantities are given by

$$O = \frac{1}{N_{\mathrm{smp}}}\sum_{n=1}^{N_{\mathrm{smp}}} O(t_0+n\Delta), \tag{8}$$

with the number of samples N_{smp} and the time step Δ. The typical values of t_0, N_{smp}, and Δ are set to $t_0 = 800T$, $N_{\mathrm{smp}} = 20000$, and $\Delta = 0.02T$, respectively.

IV. RESULTS

In the following simulations, we choose $J_1 = 1$ and $J_3 = -0.5$ with $Q^* = 2\pi/5$; the ground-state energy per site is given by $E_{\mathrm{gs}} = -J_1[\cos Q^* + 2\cos(Q^*/2)] - J_3[\cos(2Q^*) + 2\cos Q^*]$, whose absolute value is taken as the energy-scale unit. We set $\gamma = 1$ and $\alpha_{\mathrm{G}} = 0.05$. The LLG equation is solved by using the open software DifferentialEquations.jl [57]. The time scale is set as $|E_{\mathrm{gs}}|^{-1}$. We consider the system consisting of $N = 20^2$ spins under the periodic boundary conditions; we have confirmed that qualitatively similar results have been obtained for larger system sizes, e.g., $N = 40^2$. In the following, we focus on the high-frequency regime, where the frequency ω is large enough compared to the static energy scale $|E_{\mathrm{gs}}|$; we fix $\omega/|E_{\mathrm{gs}}| = 7.5$. Similar results have been obtained for other frequencies; the comparison results are summarized in Appendix A. Hereafter, we exhibit results for the RCP electric field. Results for the LCP electric field are shown in Appendix B.

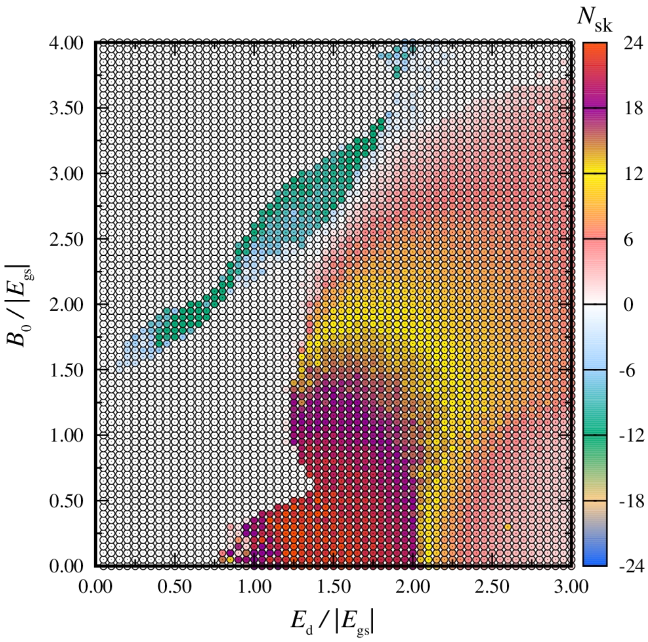

FIG. 1. Averaged skyrmion number N_{sk} as functions of E_{d} and B_0 at $\omega/|E_{\mathrm{gs}}| = 7.5$ in the NESSs under the RCP electromagnetic field.

A. Circularly polarized electromagnetic fields

First, we demonstrate that the competition between electric- and magnetic-field-induced effective interactions leads to a qualitative change in the topology of the NESS, resulting in a transition between SkXs with different skyrmion numbers. We consider the situation where the circularly polarized electromagnetic field is applied in the absence of the static magnetic field, namely, $B_{\mathrm{s}}^z = 0$. As an initial spin configuration, we adopt the single-Q spiral state, which corresponds to the ground state at $E_0 = B_0 = 0$; we choose the spiral plane as the xy plane, as the qualitatively similar results are obtained for the

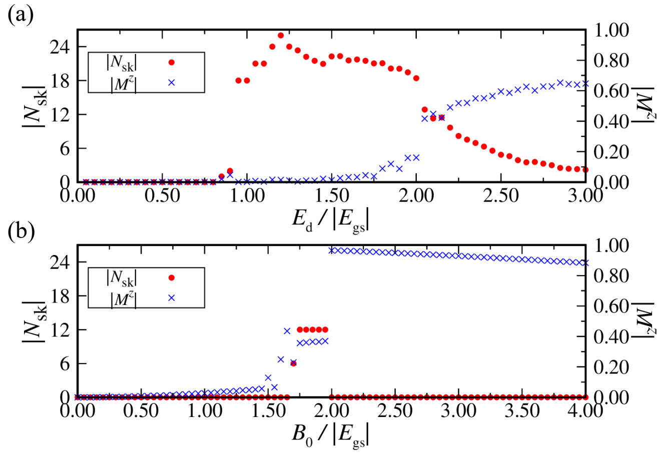

FIG. 2. (a) $E_{\rm d}$ dependence of the absolute $N_{\rm sk}$ and averaged absolute out-of-plane magnetization M^z at $B_0/E_{\rm d} = 0.2$. (b) B_0 dependence of the absolute $N_{\rm sk}$ and the absolute M^z at $B_0/E_{\rm d} = 3.6$.

other spiral planes.

Figure 1 shows the averaged skyrmion number $N_{\rm sk}$ as functions of the strength of the RCP electric field $E_{\rm d} = \lambda E_0$ and the RCP magnetic field B_0 in the NESSs; the skyrmion number becomes nonzero in a wide range of electromagnetic-field parameters, indicating the emergence of topological spin textures, i.e., the SkXs. Across the line $B_0/E_{\rm d} = 1$, the sign of the skyrmion number tends to be reversed; $N_{\rm sk} > 0$ for $B_0/E_{\rm d} < 1$ and $N_{\rm sk} < 0$ for $B_0/E_{\rm d} > 1$. Meanwhile, the stability region of the SkXs is asymmetric in terms of $B_0/E_{\rm d} = 1$, with the RCP electric field being more favorable than the RCP magnetic field. Indeed, the SkX phase is stabilized around $1 \le E_{\rm d}/|E_{\rm gs}| \le 1.6$ solely by the RCP electric field even at $B_0 = 0$, whereas no SkX phase appears only by the RCP magnetic field at $E_{\rm d} = 0$. These results indicate that the RCP electric field induces a SkX with a positive skyrmion number, whereas the addition of an RCP magnetic field reverses the sign, leading to a SkX with a negative skyrmion number.

The detailed dependence on B_0 and $E_{\rm d}$ at fixed $B_0/E_{\rm d} = 0.2$ or $B_0/E_{\rm d} = 3.6$ is presented in Fig. 2. When the electric-field effect is dominant compared to the magnetic-field one ($B_0 < E_{\rm d}$), the SkXs with $+18 \lesssim N_{\rm sk} \lesssim +24$ are induced, as shown in Fig. 2(a). The snapshot of the spin configuration of the SkX with $N_{\rm sk} = +24$ is shown in the left panel of Fig. 3(a). This SkX consists of the skyrmion with $n_{\rm sk} = +2$ [49]; it has the positive scalar spin chirality and the superpositions of the ordering wave vectors $\boldsymbol{Q}_1^*$, $\boldsymbol{Q}_2^*$, and $\boldsymbol{Q}_3^*$, as shown in the middle and right panels of Fig. 3(a). Notably, the stabilization of the SkX with $n_{\rm sk} = +2$ in a driven dissipative system is nontrivial, as higher-order skyrmions are not generically realized without additional mechanisms. This result highlights a distinct non-equilibrium route to higher-topological-number SkXs. The sign of the scalar spin chirality is determined by the polarization of the light (δ). Similarly, the SkX with $N_{\rm sk} = +18$ also corresponds to the periodic alignment of the skyrmions with $n_{\rm sk} = +2$, although the positions of the triple-Q ordering wave vectors are located at $(\boldsymbol{Q}_1^* - \boldsymbol{Q}_3^*)/2$, $(\boldsymbol{Q}_2^* - \boldsymbol{Q}_1^*)/2$, and $(\boldsymbol{Q}_3^* - \boldsymbol{Q}_2^*)/2$. Such SkXs with $n_{\rm sk} = +2$ have also been reported in equilibrium systems by introducing multi-spin interactions [58–61] and magnetic anisotropic interactions [62–67] in addition to the frustrated exchange interactions, suggesting that the RCP electric field effectively mimics these interactions in a dynamical manner, as discussed below [49].

In the other region for $E_{\rm d} > B_0$ in Fig. 1, the SkX with quantized skyrmion number is not clearly observed; for example, around $B_0/|E_{\rm gs}| \simeq 2.15$ and $E_{\rm d}/|E_{\rm gs}| \simeq 1.65$, the SkX with $N_{\rm sk} \sim +12$ is obtained. We regard this state as a transient state of the melting of the topological spin textures from the SkXs with $N_{\rm sk} = +24$ and $N_{\rm sk} = +18$ to the topologically trivial state without $N_{\rm sk}$ [49]. Indeed, its spin structure factor exhibits a broadened peak structure rather than a sharp one shown in the right panel of Fig. 3.

On the other hand, the situation where the magnetic-field effect is dominant ($B_0 > E_{\rm d}$) leads to the instability toward the another SkX with the skyrmion number $N_{\rm sk} = -12$, as shown in the case of $B_0/|E_{\rm gs}| \sim 1.8$ in Fig. 2(b). It consists of the Bloch-type skyrmion with $n_{\rm sk} = -1$ with a definite helicity and vorticity, as shown in the left panel of Fig. 3(b); it has the negative scalar spin chirality at the core and peaks at $\boldsymbol{q} = \boldsymbol{0}$ in addition to the ordering wave vectors $\boldsymbol{Q}_1^*$, $\boldsymbol{Q}_2^*$, and $\boldsymbol{Q}_3^*$, as shown in the middle and right panels of Fig. 3(b). This SkX with $n_{\rm sk} = -1$ has been found in centrosymmetric magnets even without the dynamical electromagnetic fields, but other effects, such as the thermal fluctuations [37, 68] and single-ion anisotropy [39–42], are additionally taken into account. In other words, the dynamical electromagnetic fields play a similar role in these effects.

To gain qualitative insight into the emergence of the SkXs obtained in the NESSs, we introduce an effective static spin Hamiltonian based on the Floquet formalism [51, 52, 69, 70]. However, it should be noted that the actual steady states arise from the interplay between time-dependent driving and dissipative dynamics, which cannot be fully captured by a purely static effective Hamiltonian. The effect of the time-periodic field is perturbatively incorporated into a time-independent Floquet Hamiltonian up to the lowest order of ω^{-1}, which is given by [52]

$$
\begin{aligned}
\mathcal{H}_{\rm F} = \mathcal{H}_{\rm static} &+ \boldsymbol{\mathcal{B}} \cdot \sum_i \boldsymbol{S}_i + \mathcal{D} \sum_i \sum_{\alpha=1,2,3} \boldsymbol{e}_\alpha \cdot (\boldsymbol{S}_i \times \boldsymbol{S}_{i+\boldsymbol{e}_\alpha}) \\
&+ \mathcal{T} \sum_i \sum_{\sigma=\pm 1} S_i^z \, (\boldsymbol{S}_{j+\sigma \boldsymbol{e}_1} \times \boldsymbol{S}_{j+\sigma \boldsymbol{e}_2} \\
&+ \boldsymbol{S}_{j+\sigma \boldsymbol{e}_2} \times \boldsymbol{S}_{j+\sigma \boldsymbol{e}_3} + \boldsymbol{S}_{j+\sigma \boldsymbol{e}_3} \times \boldsymbol{S}_{j+\sigma \boldsymbol{e}_1})^z \\
&+ \mathcal{T} \sum_{\triangle, \triangledown} \boldsymbol{S}_i \cdot (\boldsymbol{S}_j \times \boldsymbol{S}_k) \,,
\end{aligned} \tag{9}
$$

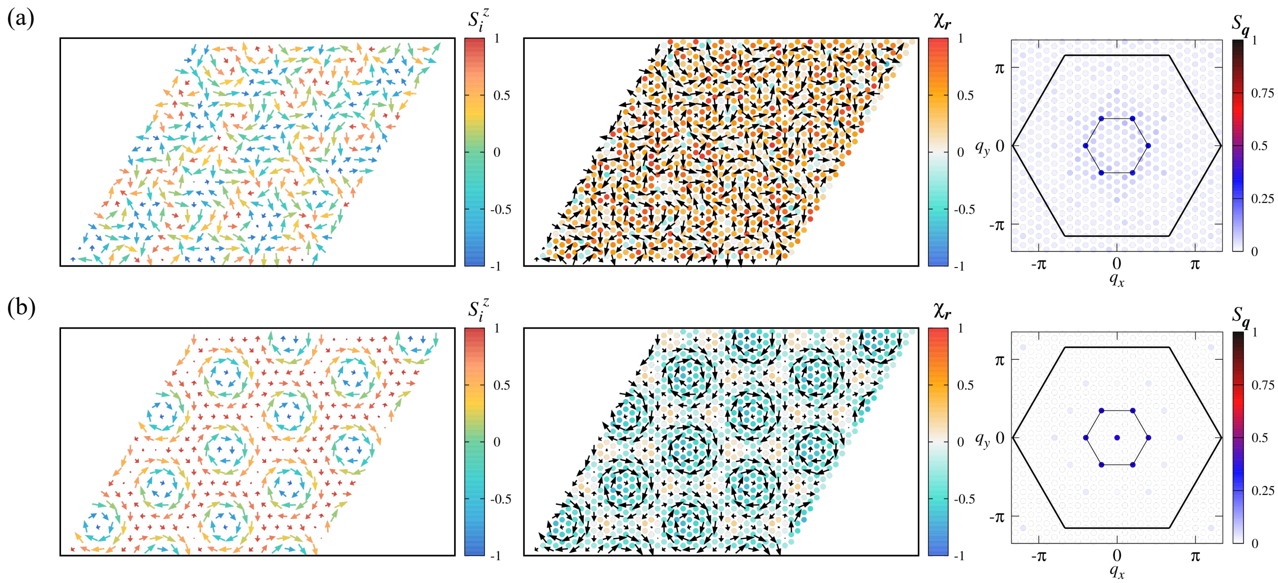

FIG. 3. Snapshots of the NESSs under the RCP electric field with $\omega/|E_{\rm gs}| = 7.5$; (a) $(E_{\rm d}/|E_{\rm gs}|, B_0/|E_{\rm gs}|) = (1.25, 0.25)$ and (b) $(E_{\rm d}/|E_{\rm gs}|, B_0/|E_{\rm gs}|) = (0.5, 1.8)$. (Left panels) Real-space spin configurations; the arrows and color denote the spins $\boldsymbol{S}_i$ and the z component S_i^z, respectively. (Middle panels) Local scalar spin chirality configurations; the arrows and color of the circles denote the spins $\boldsymbol{S}_i$ and the local scalar spin chirality $\chi_{\boldsymbol{r}}$, respectively. (Right panels) Reciprocal-space spins $S_{\boldsymbol{q}}$. The large hexagons represent the first Brillouin zone. The vertices of the small hexagons correspond to $\pm\boldsymbol{Q}_1^*$, $\pm\boldsymbol{Q}_2^*$, and $\pm\boldsymbol{Q}_3^*$.

with

$$\boldsymbol{\mathcal{B}} = \frac{\delta B_0^2}{2\omega}\boldsymbol{e}_z, \tag{10}$$

$$\mathcal{D} = \frac{\delta E_0 B_0 \lambda}{2\omega}, \tag{11}$$

and

$$\mathcal{T} = -\frac{\sqrt{3}\delta E_0^2 \lambda^2}{4\omega}. \tag{12}$$

The first term $\mathcal{H}_{\rm static}$ consists of the spin Hamiltonian $\mathcal{H}_0$ and the Zeeman coupling to the static magnetic field, and the other terms arise from the dynamical electromagnetic fields. The second term in Eq. (9) is the effective Zeeman coupling to the circularly polarized magnetic field proportional to B_0^2; $\boldsymbol{e}_z$ in Eq. (10) is the unit vector in the perpendicular direction to the xy plane. The third term in Eq. (9) represents the effective field-induced chiral DM interaction arising from the coupling between electric and magnetic fields [51]; $\boldsymbol{e}_1 = (1, 0)$, $\boldsymbol{e}_2 = (1/2, \sqrt{3}/2)$, and $\boldsymbol{e}_3 = (-1/2, \sqrt{3}/2)$ are the vectors of the nearest-neighbor bonds. The last two terms represent effective three-spin interactions induced by the second order of the electric field E_0^2 [49], where the summation in the last term runs over both upward and downward unit triangles and the sites (i, j, k) are labeled in a counterclockwise order.

The effective interactions appearing in Eq. (9) provide the reason why the SkXs with $n_{\rm sk} = +2$ and $n_{\rm sk} = -1$ are stabilized under dynamical electromagnetic fields intuitively. The SkX with $n_{\rm sk} = +2$, which emerges even in the absence of B_0, as shown in Fig. 2(a), is attributed to the effective three-spin interactions that originate from the time-dependent electric field [49]. This is understood from the fact that the coupling form in the three-spin interaction terms naturally favors noncoplanar spin textures with a finite scalar spin chirality. Since the effective three-spin interaction depends on the light polarization δ, the favorable sign of the scalar spin chirality is determined by δ; the RCP with $\delta = +1$ (LCP with $\delta = -1$) selects the state with the positive (negative) scalar spin chirality. This is why the SkX with $n_{\rm sk} = +2$ is stabilized in the region for $B_0 < E_{\rm d}$.

Meanwhile, the emergence of the SkXs with $n_{\rm sk} = -1$ stabilized in the region for $B_0 > E_{\rm d}$ in Fig. 2(b) is qualitatively understood from the interplay between the effective Zeeman coupling and the effective chiral DM interactions, which becomes the origin of the magnetic-field-induced SkX, as found in static systems in noncentrosymmetric environments [8, 11, 13]. Thus, the circularly polarized electromagnetic fields mimic the situation in noncentrosymmetric chiral magnets when the magnetic-field effect is relatively dominant. Furthermore, the Bloch-type helicity around the skyrmion core is naturally understood from the direction of the DM vector, which is parallel to the nearest-neighbor bond direction.

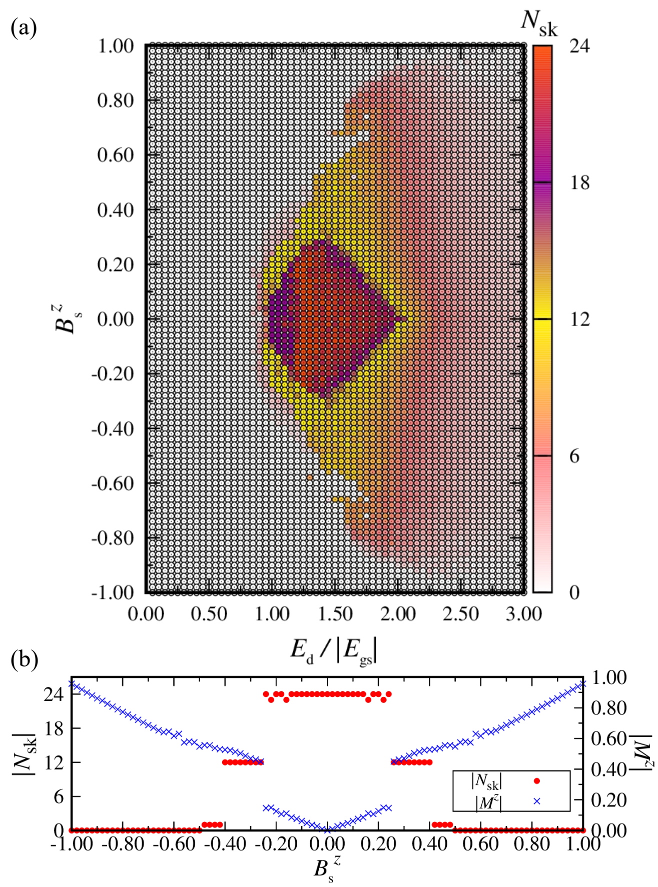

FIG. 4. (a) Averaged skyrmion number N_{sk} as functions of E_{d} and B_{s}^z at $\omega/|E_{\mathrm{gs}}| = 7.5$ in the NESSs under the RCP electric field and the static magnetic field. (b) B_{s}^z dependence of the absolute N_{sk} and the absolute M^z at $E_{\mathrm{d}}/|E_{\mathrm{gs}}| = 1.25$.

B. Circularly polarized electric fields and static magnetic fields

Next, we study the NESSs by considering the effect of the static magnetic field rather than the circularly polarized magnetic field, namely, $B_0 = 0$. In other words, we consider the situation where the effect of the circularly polarized magnetic field is ignored by supposing $B_0 \ll E_{\mathrm{d}}$. Similar to the previous case in Sec. IV A, we adopt the same initial spin configuration represented as the single-Q spiral state.

Figure 4(a) shows the averaged skyrmion number N_{sk} as functions of the strength of the RCP electric field E_{d} and the static magnetic field B_{s}^z in the NESSs. Induced topological spin textures appearing in the region around $1 \lesssim E_{\mathrm{d}}/|E_{\mathrm{gs}}| \lesssim 1.6$ uniformly exhibit the positive sign of the skyrmion number irrespective of the presence or absence of B_{s}^z and the magnetic-field directions, i.e., $N_{\mathrm{sk}} > 0$. Thus, different from Sec. IV A, the SkX with the negative skyrmion number is not stabilized under the RCP electric field and the static magnetic field. It is noted that the sign of the skyrmion number is reversed by the polarization of the light, as shown in Appendix B.

The B_{s}^z dependence of the skyrmion number and the magnetization at $E_{\mathrm{d}} = 1.25$ is shown in Fig. 4(b). For $|B_{\mathrm{s}}^z| \lesssim 0.24$, the SkXs with $N_{\mathrm{sk}} = +24$, which consist of the periodic array of the skyrmions with $n_{\mathrm{sk}} = +2$, are stabilized, similar to Sec. IV A. By increasing $|B_{\mathrm{s}}^z|$, the skyrmion number decreases from +24 to +12. The left panels of Fig. 5 show real-space spin configurations of the SkXs with $N_{\mathrm{sk}} = +12$, which correspond to the periodic alignment of the skyrmions with $n_{\mathrm{sk}} = +1$ at $|B_{\mathrm{s}}^z| = 0.3$. The signs of the scalar spin chirality and the spins in reciprocal space shown in the middle and right panels of Fig. 5, in addition to the skyrmion numbers, are the same irrespective of the magnetic-field directions. However, the real-space spin configuration seems to be different, as compared in the left panels of Figs. 5(a) and 5(b). The skyrmion core is identified as the region with $S_i^z = -1$ and is characterized by the vorticity -1 for $B_{\mathrm{s}}^z > 0$, as shown in Fig. 5(a). On the other hand, the skyrmion core is located at the region with $S_i^z = +1$ and is characterized by the vorticity +1 for $B_{\mathrm{s}}^z < 0$, as shown in Fig. 5(b). Since both polarization and vorticity take opposite signs for the two situations, both spin configurations are characterized by the same sign of the skyrmion number and the scalar spin chirality, as shown in the middle panel of Figs. 5(a) and 5(b). With a further increase of the magnetic field $|B_{\mathrm{s}}^z|$, the SkXs turn into the topologically trivial states without N_{sk}.

We discuss the microscopic origin of the SkXs under the static magnetic field based on the Floquet Hamiltonian in Eqs. (9)–(12). In contrast to the circularly polarized magnetic field, only the fourth and fifth terms are present; the effective chiral DM interaction is absent owing to $B_0 = 0$. When the static magnetic field is small, the SkX with $N_{\mathrm{sk}} = +24$ is stabilized by the effective three-spin interactions, similar to the case in Sec. IV A. Meanwhile, the emergence of the SkX with $N_{\mathrm{sk}} = +12$ is attributed to the interplay between the effective three-spin interactions and the Zeeman coupling to the static magnetic field; the former tends to favor a triple-Q spin configuration and the latter tends to favor a superposition of spiral waves rather than the sinusoidal waves [64]. Without two-spin in-plane magnetic anisotropy, the helicity and vorticity of the skyrmion core are not uniquely determined in this situation. In addition, the favorable sign of the skyrmion number is determined by the light polarization. Thus, the sign of the skyrmion number in the magnetic-field-induced SkX is affected by the light polarization, with the LCP electric field, rather than the RCP one, leading to the SkXs with the negative skyrmion number.

The stability region of the magnetic-field-induced SkX with $N_{\mathrm{sk}} = +12$ is strongly affected by the timing of the application of the RCP electric field and the static magnetic field. This result indicates that the resulting steady state is not uniquely determined by the instantaneous Hamiltonian, but depends on the dynamical pathway toward the NESS. To demonstrate this, we perform

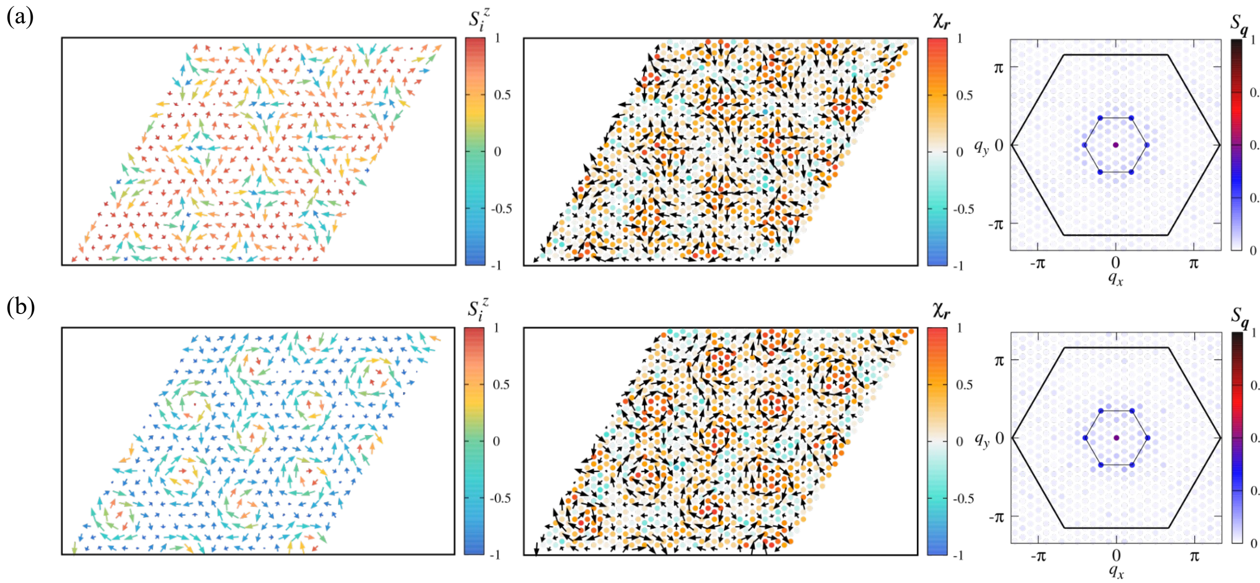

FIG. 5. Snapshots of the NESSs under the RCP electric field with $\omega/|E_{\rm gs}| = 7.5$; (a) $(E_{\rm d}/|E_{\rm gs}|, B_{\rm s}^z) = (1.25, 0.3)$ and (b) $(E_{\rm d}/|E_{\rm gs}|, B_{\rm s}^z) = (1.25, -0.3)$. (Left panels) Real-space spin configurations; the arrows and color denote the spins $\boldsymbol{S}_i$ and the z component S_i^z, respectively. (Middle panels) Local scalar spin chirality configurations; the arrows and color of the circles denote the spins $\boldsymbol{S}_i$ and the local scalar spin chirality $\chi_{\boldsymbol{r}}$, respectively. (Right panels) Reciprocal-space spins $S_{\boldsymbol{q}}$. The large hexagons represent the first Brillouin zone. The vertices of the small hexagons correspond to $\pm\boldsymbol{Q}_1^*$, $\pm\boldsymbol{Q}_2^*$, and $\pm\boldsymbol{Q}_3^*$.

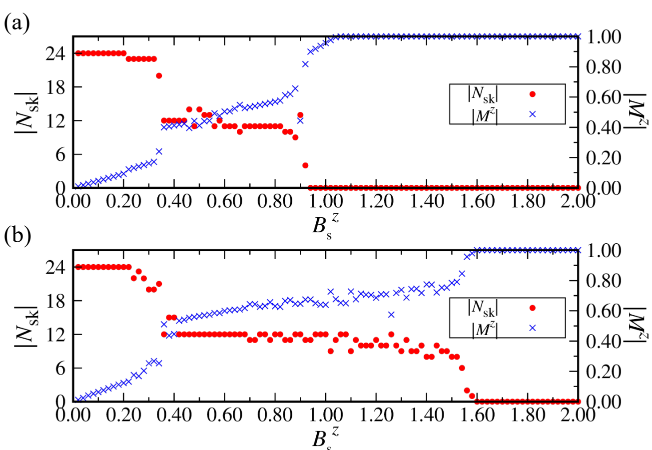

FIG. 6. $B_{\rm s}^z$ dependence of the absolute $N_{\rm sk}$ and averaged absolute M^z under the static magnetic field at $E_{\rm d}/|E_{\rm gs}| = 1.25$. The results in (a) and (b) stand for absence and presence of the RCP electric field with $\omega/|E_{\rm gs}| = 7.5$ after the system reaches the NESS without the magnetic field, respectively.

the following setups. First, we obtain the NESS under the RCP electric field at $E_{\rm d}/|E_{\rm gs}| = 1.25$ by adopting the single-Q spiral configuration with the spiral plane in the xy plane as the initial one. Subsequently, a static magnetic field is applied to the NESS, and two situations are examined: (i) the RCP electric field is turned off, and (ii) the RCP electric field remains applied. The former and latter results as a function of $B_{\rm s}^z$ are summarized in Figs. 6(a) and 6(b), respectively. The simulations are independently performed for different $B_{\rm s}^z$.

As shown in Figs. 6(a) and 6(b), both results show the topological phase transition between the SkXs with $N_{\rm sk} = +24$ and $N_{\rm sk} = +12$ at $B_{\rm s}^z \simeq 0.36$. Meanwhile, the stability region of the SkX with $N_{\rm sk} = +12$ is substantially extended when the RCP electric field is kept. This tendency can be attributed to the effective three-spin interactions induced by the RCP electric field, which enhance the stability of spin configurations with finite scalar spin chirality, such as the SkX. However, the critical magnetic field of the transition between the SkXs with $N_{\rm sk} = +24$ and $N_{\rm sk} = +12$ is not affected by the presence or absence of the RCP electric field, which implies that the higher-order SkX possessing large magnetization $|M^z|$ becomes energetically unstable, resulting in the phase transition to another SkX.

Moreover, compared to Fig. 4(b), where both the RCP electric field and the static magnetic field are simultaneously applied at $t = 0$, both the SkXs with $N_{\rm sk} = +24$ and $N_{\rm sk} = +12$ are more stabilized in the present setup. In the previous setup, the topological phase transition between the SkXs with $N_{\rm sk} = +24$ and $N_{\rm sk} = +12$ ($N_{\rm sk} = +12$ and $N_{\rm sk} \sim 0$) occurs at $B_{\rm s}^z \simeq 0.26$ ($B_{\rm s}^z \simeq 0.42$), whereas the larger magnetic fields are required to obtain the same topological phase transitions as shown in Fig 6. This features the robustness of topological spin textures against the external fields once they are generated. Thus, the timing of the application of the RCP electric field and the static magnetic field plays a crucial role in determining the final topological state. This highlights a characteristic feature of driven non-equilibrium systems, where the NESS properties depend on the temporal protocol rather than solely on the Hamiltonian parameters. Such path-dependent stabilization has no direct counterpart in equilibrium systems.

V. SUMMARY AND DISCUSSION

TABLE I. The classification of the skyrmion number within the magnetic unit cell $n_{\rm sk}$ under time-dependent electromagnetic fields and the static magnetic field. We omit the SkX with $n_{\rm sk} = \pm 2$ under the circularly polarized or static magnetic fields.

Magnetic field \ Electric field	RCP ($\delta = +1$)	LCP ($\delta = -1$)
No magnetic fields	$+2$	-2
RCP ($\delta = +1$)	-1	–
LCP ($\delta = -1$)	–	$+1$
$B_{\rm s}^z > 0$	$+1$	-1
$B_{\rm s}^z < 0$	$+1$	-1

We have theoretically investigated NESSs in frustrated magnets driven by time-dependent electromagnetic fields, focusing on the stability and topological transitions of SkXs with different skyrmion numbers. Our analysis is based on a classical Heisenberg model on the two-dimensional triangular lattice, where the electric field couples to spins via the inverse DM mechanism. By numerically solving the LLG equation, we have examined two representative setups of external magnetic fields in addition to the circularly polarized electric field: one is a circularly polarized magnetic field and the other is a static magnetic field.

Starting from a single-Q spiral state, we have demonstrated that time-dependent electromagnetic fields induce a variety of SkXs as NESSs, including those with higher skyrmion numbers such as $n_{\rm sk} = +2$. Importantly, the emergence of these topological states is governed by the interplay between dynamical driving and dissipative dynamics, rather than being solely determined by an effective static Hamiltonian. We find that distinct SkXs are selectively stabilized depending on the relative contributions of the electric and magnetic fields: the RCP electric field favors the SkX with $n_{\rm sk} = +2$, while the magnetic-field-induced SkXs exhibit different topological numbers depending on the field configuration, such as $n_{\rm sk} = -1$ under a circularly polarized magnetic field and $n_{\rm sk} = +1$ under a static magnetic field. These results can be qualitatively interpreted by effective interactions derived from the Floquet formalism; however, the actual steady states reflect intrinsically dynamical processes beyond such static descriptions. We summarize the relationship between the sign of the skyrmion number in the SkX and the applied electromagnetic fields in Table I.

Furthermore, we have shown that the resulting SkX phases depend sensitively on the temporal protocol of the applied fields. In particular, the stability regions are significantly modified by the timing of the electric and magnetic fields, indicating that the final topological state is path-dependent. This highlights a key feature of driven non-equilibrium systems, where NESSs are not uniquely determined by Hamiltonian parameters alone. Our findings provide a unified framework for understanding and controlling topological spin textures under time-dependent electromagnetic fields, offering a route to dynamically engineer SkXs beyond conventional equilibrium mechanisms.

Finally, we briefly comment on the validity of our results. We have focused on the parameter regime where the single-Q spiral state is stabilized as the ground state under an external static magnetic field. This indicates that the time-dependent electromagnetic fields play an essential role in inducing various types of SkXs. At a quantitative level, assuming typical exchange interaction energy of 1–10 meV, the relevant frequency lies in the THz regime. The corresponding field strengths are estimated to be 1–100 T for magnetic fields and 10–100 MV/cm for electric fields. In this regime, heating effects due to electromagnetic-wave absorption are expected to be smaller than the characteristic energy scales considered here, although a more quantitative treatment of heating remains an important future issue. Therefore, simulations based on the LLG equation without including heating effects are sufficient to describe the spin dynamics under THz fields [51, 71–73]. For typical electric polarization values of $|\boldsymbol{p}| \sim$ 1–100 μC/m^2 in multiferroic materials [45], the parameter $E_{\rm d}$ is estimated to be $10^{-5}E_0$–$10^{-3}E_0$ meV for the volume of the unit cell 100 Å^3. Our results are expected to be valid below the transition temperature in multiferroic systems hosting the single-Q spiral state, providing insights into both the fundamental understanding and potential manipulation of topological spin structures in optically driven multiferroic magnets with strong magnetoelectric coupling.

ACKNOWLEDGMENTS

This research was supported by JSPS KAKENHI Grants Numbers JP22H00101, JP22H01183, JP23H04869, JP23K03288, JP23K20827, and by JST CREST (JPMJCR23O4) and JST FOREST (JPMJFR2366).

Appendix A: Frequency dependence of the topological phase transitions

We present the results for the NESSs at $\omega/|E_{\rm gs}| = 7.5$ in Sec. IV. Similar results are obtained even when we consider other frequencies on both setups in terms of dynamical and static magnetic fields, which indicates robustness of our results in the high-frequency regime. Figures 7(a) and (b) show the results the averaged skyrmion number $N_{\rm sk}$ as functions of the strength of the RCP electric field $E_{\rm d}$ and the RCP magnetic field B_0 at $\omega/|E_{\rm gs}| = 6$ and $\omega/|E_{\rm gs}| = 8$, respectively, in the NESSs obtained by irradiating the circularly polarized electromagnetic field without the static magnetic field. Compared with the results for $\omega/|E_{\rm gs}| = 7.5$ in Fig. 1, as the frequency increases, the region with $N_{\rm sk} > 0$ ($N_{\rm sk} < 0$) shifts toward the region of higher $E_{\rm d}$ (B_0). In addition, the region with $N_{\rm sk} > 0$ ($N_{\rm sk} < 0$) extends in the direction toward higher B_0 ($E_{\rm d}$).

Meanwhile, Fig. 8 shows $N_{\rm sk}$ as functions of the frequency ω and the static magnetic field $B^z_{\rm s}$ at $E_{\rm d}/|E_{\rm gs}| = 1.25$ in the NESSs under the situation where the effect of the circularly polarized magnetic field is ignored. At the fixed $E_{\rm d}$, as the frequency increases, the corresponding skyrmion number also increases in the range from $\omega/|E_{\rm gs}| = 6$ to $\omega/|E_{\rm gs}| = 7.5$; however, the skyrmion number decreases when the frequency changes from $\omega/|E_{\rm gs}| = 7.5$ to $\omega/|E_{\rm gs}| = 8$. This tendency suggests that the region with $N_{\rm sk} > 0$ shifts toward the region of higher $E_{\rm d}$, similar to the case applying the RCP electromagnetic field without the static magnetic field.

Appendix B: Case of the left circularly polarized electric field

In Sec. IV, we present the results under the RCP electric field. Since the LCP electric field in combination with the magnetic fields leads to the same magnitude of the effective interaction but with a different sign, the stability region of the SkXs is not altered. Meanwhile, the sign of the skyrmion number is reversed. The results for representative parameters are shown in Fig. 9, where Figs. 9(a,b) [Figs. 9(c,d)] present the case under the LCP electromagnetic field (the combination of the LCP electric field and the static magnetic field). In each case, the SkXs with the opposite skyrmion number to those obtained under the RCP fields are generated.

[1] J. M. Kosterlitz and D. J. Thouless, J. Phys. C **6**, 1181 (1973).
[2] J. M. Kosterlitz, J. Phys. C **7**, 1046 (1974).
[3] D. J. Thouless, M. Kohmoto, M. P. Nightingale, and M. den Nijs, Phys. Rev. Lett. **49**, 405 (1982).
[4] M. Kohmoto, Ann. Phys. (N.Y.) **160**, 343 (1985).
[5] T. H. R. Skyrme, Nucl. Phys. **31**, 556 (1962).
[6] A. N. Bogdanov and D. A. Yablonskii, Sov. Phys. JETP **68**, 101 (1989).
[7] A. Bogdanov and A. Hubert, J. Magn. Magn. Mater. **138**, 255 (1994).
[8] U. K. Rößler, A. N. Bogdanov, and C. Pfleiderer, Nature **442**, 797 (2006).
[9] N. Nagaosa and Y. Tokura, Nat. Nanotech. **8**, 899 (2013).
[10] X. Zhang, Y. Zhou, K. M. Song, T.-E. Park, J. Xia, M. Ezawa, X. Liu, W. Zhao, G. Zhao, and S. Woo, J. Phys.: Condens. Matter **32**, 143001 (2020).
[11] Y. Tokura and N. Kanazawa, Chem. Rev. **121**, 2857 (2021).
[12] S. Hayami and Y. Motome, J. Phys.: Condens. Matter **33**, 443001 (2021).
[13] S. Hayami and R. Yambe, Mater. Today Quantum **3**, 100010 (2024).
[14] M. V. Berry, Proc. R. Soc. Lond. A **392**, 45 (1984).
[15] D. Loss and P. M. Goldbart, Phys. Rev. B **45**, 13544 (1992).
[16] J. Ye, Y. B. Kim, A. J. Millis, B. I. Shraiman, P. Majumdar, and Z. Tešanović, Phys. Rev. Lett. **83**, 3737 (1999).
[17] K. Ohgushi, S. Murakami, and N. Nagaosa, Phys. Rev. B **62**, R6065 (2000).
[18] R. Shindou and N. Nagaosa, Phys. Rev. Lett. **87**, 116801 (2001).
[19] A. Neubauer, C. Pfleiderer, B. Binz, A. Rosch, R. Ritz, P. G. Niklowitz, and P. Böni, Phys. Rev. Lett. **102**, 186602 (2009).
[20] X. Z. Yu, N. Kanazawa, W. Z. Zhang, T. Nagai, T. Hara, K. Kimoto, Y. Matsui, Y. Onose, and Y. Tokura, Nat. Commun. **3**, 988 (2012).
[21] T. Yokouchi, S. Sugimoto, B. Rana, S. Seki, N. Ogawa, Y. Shiomi, S. Kasai, and Y. Otani, Sci. Adv. **8**, eabq5652 (2022).
[22] O. Lee, T. Wei, K. D. Stenning, J. C. Gartside, D. Prestwood, S. Seki, A. Aqeel, K. Karube, N. Kanazawa, Y. Taguchi, C. Back, Y. Tokura, W. R. Branford, and H. Kurebayashi, Nat. Mater. **23**, 79 (2024).
[23] G. Tanaka, T. Yamane, J. B. Héroux, R. Nakane, N. Kanazawa, S. Takeda, H. Numata, D. Nakano, and A. Hirose, Neural Netw. **115**, 100 (2019).
[24] S. Mühlbauer, B. Binz, F. Jonietz, C. Pfleiderer, A. Rosch, A. Neubauer, R. Georgii, and P. Böni, Science **323**, 915 (2009).
[25] T. Adams, S. Mühlbauer, C. Pfleiderer, F. Jonietz, A. Bauer, A. Neubauer, R. Georgii, P. Böni, U. Keiderling, K. Everschor, M. Garst, and A. Rosch, Phys. Rev. Lett. **107**, 217206 (2011).
[26] X. Z. Yu, Y. Onose, N. Kanazawa, J. H. Park, J. H. Han, Y. Matsui, N. Nagaosa, and Y. Tokura, Nature **465**, 901 (2010).
[27] T. Adams, S. Mühlbauer, A. Neubauer, W. Münzer, F. Jonietz, R. Georgii, B. Pedersen, P. Böni, A. Rosch, and C. Pfleiderer, in J. Phys.: Conf. Ser., Vol. 200 (IOP Publishing, 2010) p. 032001.
[28] S. D. Yi, S. Onoda, N. Nagaosa, and J. H. Han, Phys. Rev. B **80**, 054416 (2009).
[29] I. Dzyaloshinsky, J. Phys. Chem. Solids **4**, 241 (1958).
[30] T. Moriya, Phys. Rev. **120**, 91 (1960).
[31] T. Kurumaji, T. Nakajima, M. Hirschberger, A. Kikkawa, Y. Yamasaki, H. Sagayama, H. Nakao, Y. Taguchi, T. hisa Arima, and Y. Tokura,

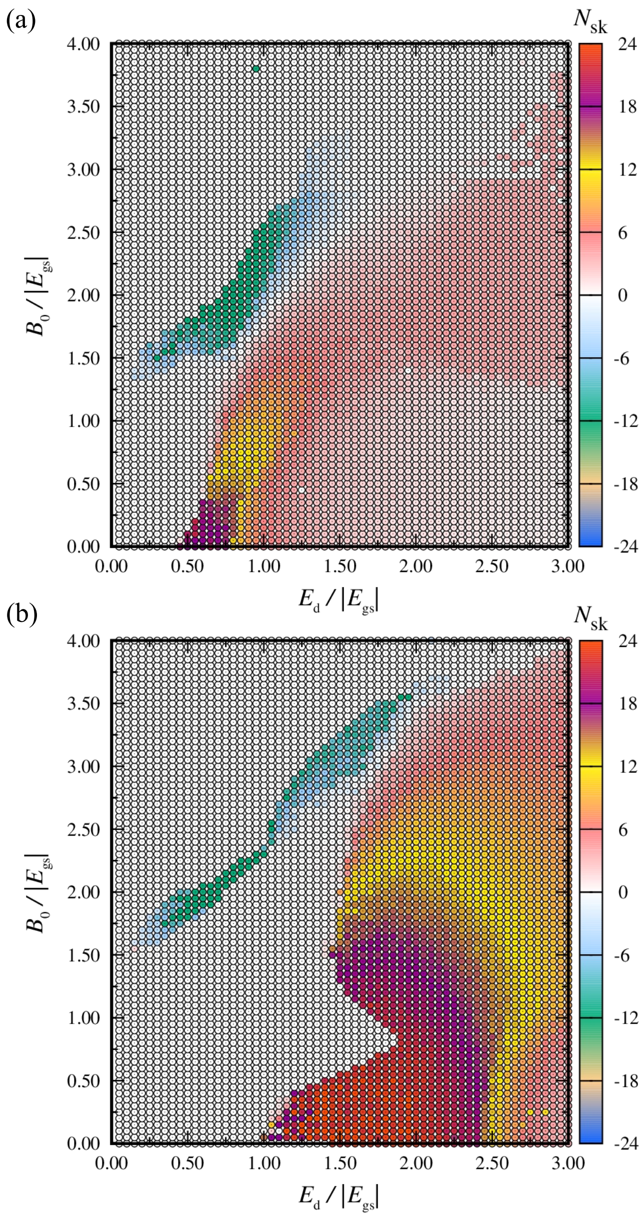

FIG. 7. Averaged skyrmion number $N_{\rm sk}$ as functions of $E_{\rm d}$ and B_0 at (a) $\omega/|E_{\rm gs}| = 6.0$ and (b) $\omega/|E_{\rm gs}| = 8.0$ in the NESSs under the RCP electromagnetic field.

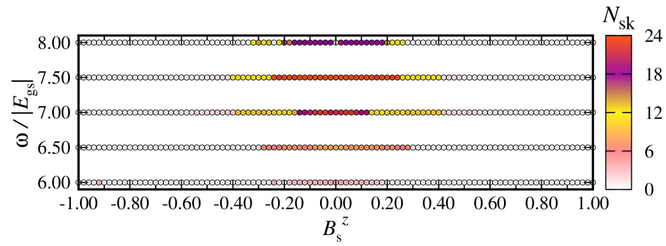

FIG. 8. Averaged skyrmion number $N_{\rm sk}$ as functions of $\omega/|E_{\rm gs}|$ and $B_{\rm s}^z$ at $E_{\rm d}/|E_{\rm gs}| = 1.25$ in the NESSs under the RCP electric field and the static magnetic field. It is noted that the results for $\omega/|E_{\rm gs}| = 7.5$ are based on the same data as in Fig. 4(b).

Science **365**, 914 (2019).
[32] M. Hirschberger, T. Nakajima, S. Gao, L. Peng, A. Kikkawa, T. Kurumaji, M. Kriener, Y. Yamasaki, H. Sagayama, H. Nakao, K. Ohishi, K. Kakurai, Y. Taguchi, X. Yu, T.-h. Arima, and Y. Tokura, Nat. Commun. **10**, 5831 (2019).
[33] M. Hirschberger, S. Hayami, and Y. Tokura, New J. Phys. **23**, 023039 (2021).
[34] M. A. Ruderman and C. Kittel, Phys. Rev. **96**, 99 (1954).
[35] T. Kasuya, Progr. Theor. Phys. **16**, 45 (1956).
[36] K. Yosida, Phys. Rev. **106**, 893 (1957).
[37] T. Okubo, S. Chung, and H. Kawamura, Phys. Rev. Lett. **108**, 017206 (2012).
[38] W. Koshibae and N. Nagaosa, Nat. Commun. **5**, 1 (2014).
[39] A. O. Leonov and M. Mostovoy, Nat. Commun. **6**, 8275 (2015).
[40] S.-Z. Lin and S. Hayami, Phys. Rev. B **93**, 064430 (2016).
[41] S. Hayami, S. Z. Lin, and C. D. Batista, Phys. Rev. B **93**, 184413 (2016).
[42] S. Hayami, Phys. Rev. B **103**, 224418 (2021).
[43] A. N. Bogdanov and D. A. Yablonskii, Sov. Phys. JETP **68**, 101 (1989).
[44] S. C. Furuya and M. Sato, Phys. Rev. Res. **6**, 013228 (2024).
[45] Y. Tokura, S. Seki, and N. Nagaosa, Rep. Prog. Phys. **77**, 076501 (2014).
[46] M. Mochizuki and Y. Watanabe, Appl. Phys. Lett. **107**, 082409 (2015).
[47] M. Mochizuki, Adv. Electron. Mater. **2**, 1500180 (2016).
[48] P. Huang, M. Cantoni, A. Kruchkov, J. Rajeswari, A. Magrez, F. Carbone, and H. M. Rønnow, Nano Lett. **18**, 5167 (2018).
[49] R. Yambe and S. Hayami, Phys. Rev. B **110**, 014428 (2024).
[50] T. Shirato, R. Yambe, and S. Hayami, J. Phys. Soc. Jpn. **94**, 063601 (2025).
[51] M. Sato, S. Takayoshi, and T. Oka, Phys. Rev. Lett. **117**, 147202 (2016).
[52] R. Yambe and S. Hayami, Phys. Rev. B **108**, 064420 (2023).
[53] H. Katsura, N. Nagaosa, and A. V. Balatsky, Phys. Rev. Lett. **95**, 057205 (2005).
[54] M. Mostovoy, Phys. Rev. Lett. **96**, 067601 (2006).
[55] I. A. Sergienko and E. Dagotto, Phys. Rev. B **73**, 094434 (2006).
[56] B. Berg and M. Lüscher, Nucl. Phys. B **190**, 412 (1981).
[57] C. Rackauckas and Q. Nie, J. Open Res. Softw. **5**, 15 (2017).
[58] R. Ozawa, S. Hayami, and Y. Motome, Phys. Rev. Lett. **118**, 147205 (2017).
[59] S. Hayami and Y. Motome, Phys. Rev. B **99**, 094420 (2019).
[60] S. Hayami, T. Okubo, and Y. Motome, Nat. Commun. **12**, 6927 (2021).

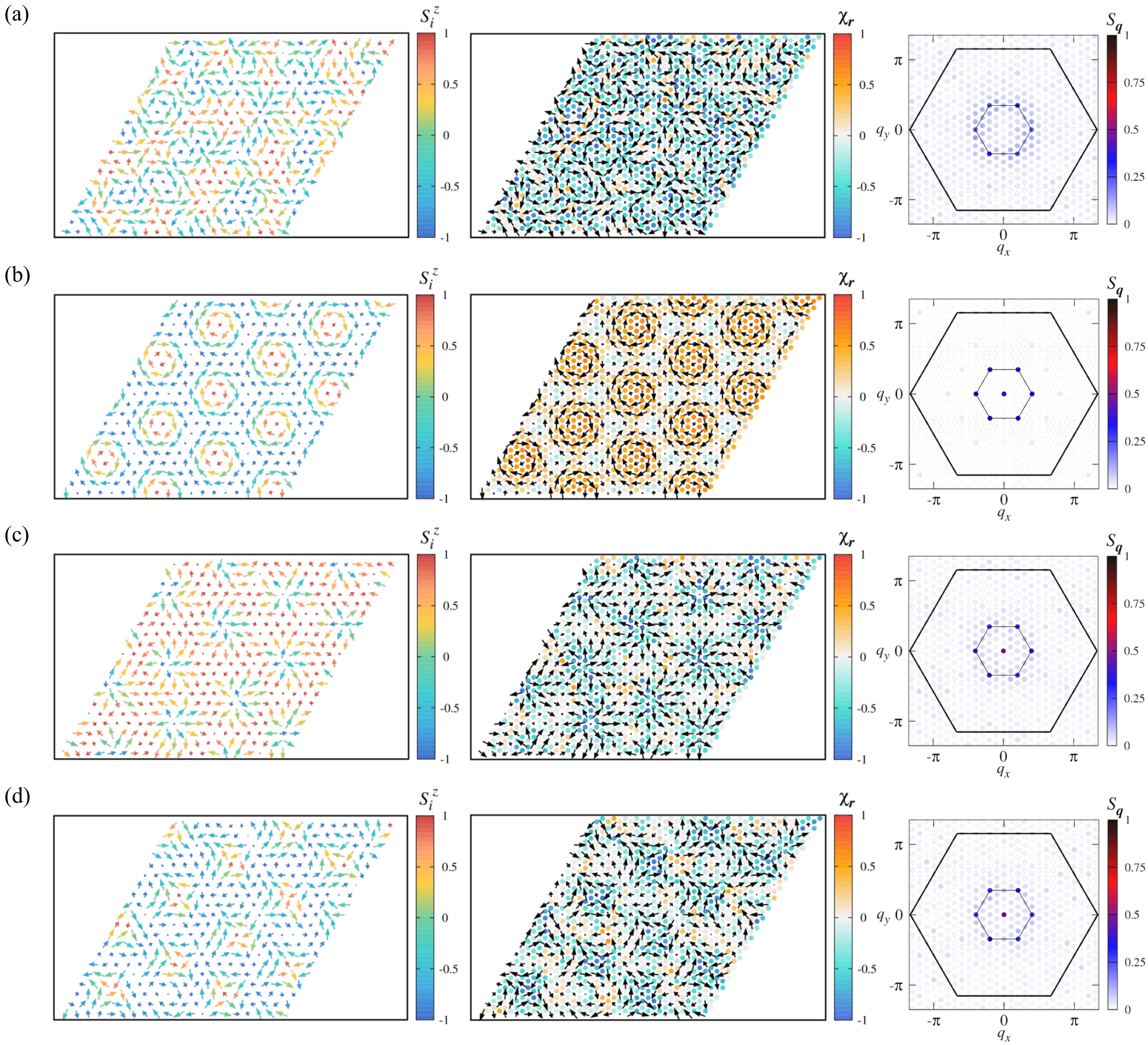

FIG. 9. Snapshots of the NESSs under the LCP electric field with $\omega/|E_{\rm gs}| = 7.5$; (a) $(E_{\rm d}/|E_{\rm gs}|, B_0/|E_{\rm gs}|, B_{\rm s}^z) = (1.25, 0.25, 0)$, (b) $(E_{\rm d}/|E_{\rm gs}|, B_0/|E_{\rm gs}|, B_{\rm s}^z) = (1.25, 1.8, 0)$, (c) $(E_{\rm d}/|E_{\rm gs}|, B_0/|E_{\rm gs}|, B_{\rm s}^z) = (1.25, 0, 0.3)$, and (d) $(E_{\rm d}/|E_{\rm gs}|, B_0/|E_{\rm gs}|, B_{\rm s}^z) = (1.25, 0, -0.3)$. (Left panels) Real-space spin configurations; the arrows and color denote the spins $\boldsymbol{S}_i$ and the z component S_i^z, respectively. (Middle panels) Local scalar spin chirality configurations; the arrows and color of the circles denote the spins $\boldsymbol{S}_i$ and the local scalar spin chirality $\chi_{\boldsymbol{r}}$, respectively. (Right panels) Reciprocal-space spins $S_{\boldsymbol{q}}$. The large hexagons represent the first Brillouin zone. The vertices of the small hexagons correspond to $\pm\boldsymbol{Q}_1^*$, $\pm\boldsymbol{Q}_2^*$, and $\pm\boldsymbol{Q}_3^*$.

[61] R. Eto and M. Mochizuki, Phys. Rev. B **104**, 104425 (2021).
[62] D. Amoroso, P. Barone, and S. Picozzi, Nat. Commun. **11**, 5784 (2020).
[63] S. Hayami and Y. Motome, Phys. Rev. B **103**, 054422 (2021).
[64] R. Yambe and S. Hayami, Sci. Rep. **11**, 11184 (2021).
[65] D. Amoroso, P. Barone, and S. Picozzi, Nanomaterials **11**, 1873 (2021).
[66] Z. Wang, Y. Su, S.-Z. Lin, and C. D. Batista, Phys. Rev. B **103**, 104408 (2021).
[67] S. Hayami, J. Phys. Soc. Jpn. **91**, 023705 (2022).
[68] K. Mitsumoto and H. Kawamura, Phys. Rev. B **105**, 094427 (2022).
[69] A. Eckardt and E. Anisimovas, New J. Phys. **17**, 093039 (2015).
[70] M. Sato and T. N. Ikeda, J. Phys. Soc. Jpn. **94**, 111007 (2025).

[71] Y. Mukai, H. Hirori, T. Yamamoto, H. Kageyama, and K. Tanaka, New J. Phys. **18**, 013045 (2016).
[72] H. Fujita and M. Sato, Phys. Rev. B **96**, 060407 (2017).
[73] Q. Zhang, S. Lin, and W. Zhang, Commun. Phys. **9**, 55 (2026).